

The NASA Solar Terrestrial Relations Observatory (STEREO) Mission Heliospheric Imager

Dennis G. Socker^{*a}, Russell A. Howard^a, Clarence M. Korendyke^a, George M. Simnett^b,
David F. Webb^c

^aNaval Research Laboratory, Washington, DC 20375

^bUniversity of Birmingham, Birmingham B15217, United Kingdom

^cBoston College, Chestnut Hill, MA 02467

ABSTRACT

The NASA Solar Terrestrial Relations Observatory (STEREO) mission will place two spacecraft into solar orbits with sufficient separation to provide remote sensing instruments with a stereoscopic view of the heliosphere extending from the lower solar corona to beyond one astronomical unit. Analysis of the stereographs returned from the two spacecraft will allow solar physicists to infer the three-dimensional structure of small and large components of the corona.

The Sun Earth Connection Coronal and Heliospheric Investigation (SECCHI) suite of remote sensing instruments includes a Heliospheric Imager (HI) to view the heliosphere in the interval from 12 to 215 solar radii. The HI will obtain the first stereographic images of coronal mass ejections in interplanetary space. Of particular interest is the subset of coronal mass ejections that propagate through the heliosphere and ultimately impact the earth. This paper presents the design concept for this new wide field coronagraph.

Keywords: coronagraph, stereoscopy, heliosphere, coronal mass ejection

1. INTRODUCTION

The NASA Solar Terrestrial Relations Observatory (STEREO) mission will place two spacecraft into nearly circular solar orbits, in the ecliptic plane, and with radii ~ 1 astronomical unit (AU). One spacecraft will lead, and the other will lag, the earth's own 1 AU orbital path and both will separate from earth at an average rate of $22^\circ/\text{year}$ over the 2-5 year mission life. The three-axis stabilized sun pointed spacecraft carry a suite of remote sensing and in situ experiments. One experiment, the Sun Earth Connection Coronal and Heliospheric Investigation (SECCHI) contains remote sensing optical systems whose overlapping fields of view will provide stereographic image pairs of the volume of space extending from the sun to the earth. The SECCHI field of view includes the lower solar corona, observed in extreme ultraviolet emission lines; the extended solar corona, normally seen in white light during total solar eclipse and with space born coronagraphs such as SOHO/LASCO; and the heliosphere out to the earth's orbit, observed in white light.

The solar corona is a magnetically structured $\sim 10^6$ °K plasma surrounding the solar photosphere. The coronal plasma density distribution can be determined with remote sensing instruments operating in the visible light regime. These instruments use broad passband filters with central wavelengths at, or near, the $\sim 5000\text{\AA}$ Planckian blackbody radiation peak associated with the ~ 5777 °K effective temperature of the solar photosphere. The "white light" images obtained through the filters measure the small fraction of the photospheric photon flux that is Thomson scattered into the line of sight by free electrons in the coronal plasma. White light images are definitive maps of the electron column density along the line of sight for each image point in a two-dimensional coronal image because Thomson scattering is both temperature and wavelength independent. The main complication arises from the optically thin nature of the scattering medium, which renders the electron density distribution along the third dimension indeterminate for single vantagepoint two-dimensional images. The STEREO mission will partially overcome this deficiency by adding a second vantagepoint. The resulting stereoscopic capability should allow the density distribution along the third dimension to be inferred with enough fidelity to address a number of outstanding and basic solar physics questions.

* Correspondence: Email: socket@lambda.nrl.navy.mil; Telephone: 202-767-2093; Fax: 202-767-5636

The most notable scientific questions to be investigated by SECCHI pertain to coronal mass ejections (CMEs). CMEs are a class of large-scale transient phenomena revealed most effectively in white light time-series observations of the corona. They are characterized by explosive and outwardly expanding coronal density fluctuations that escape the solar gravitational potential well and propagate into the heliosphere. Their rate of occurrence is about 0.8/day around solar minimum and they have velocities¹ ranging from 200-900 km/sec, an average mass $\sim 10^{15}$ gm, and an average² kinetic energy $\sim 10^{31}$ ergs. SECCHI is designed to identify the processes that initiate CMEs, determine their three-dimensional structure, measure their acceleration, study their interaction with the heliosphere and explore the details of their relationship to geomagnetic storms.

While observation of the heliosphere out to about 30 solar radii (R_{\odot}) has been accomplished with conventional coronagraphs, optical remote sensing observation of CMEs in the region of the heliosphere from 30 R_{\odot} to 215 R_{\odot} (earth orbit) has been achieved only with non-imaging instruments such as the scanning Helios zodiacal light photometers³⁻⁵. Given the STEREO mission orbital configuration (figure 1), an ideal stereoscopic imaging instrument for this region of the heliosphere would have a nearly hemispherical sun centered field of view. The SECCHI/Heliospheric Imager (HI) design concept described in this paper trades the very wide hemispheric field of view for a smaller field of view with superior sensitivity to the extremely faint and potentially geoeffective CMEs propagating within the heliospheric volume centered along the sun-earth line.

The Heliospheric Imager (HI) is designed to acquire a white light image data set suitable for stereographic reconstruction of potentially geoeffective CMEs propagating through the inner heliosphere near the sun-earth line from 12 R_{\odot} to $\sim 215 R_{\odot}$. During solar minimum, the envelope of a typical expanding CME structure (figure 2) is expected to remain within a $\sim 45^{\circ}$ cone whose axis is oriented radially outward from the sun and in the ecliptic plane. Detection of the CME signal against the natural background is a strong function of elongation (ϵ) (figure 3). The CME signal strength profile⁶ varies as R^{-2} to R^{-3} so the signal decreases about four orders of magnitude between the outer corona and $\epsilon = 90^{\circ}$. The sum of the electron corona and the dust corona (K+F) background brightness^{7,8} varies as $R^{-2.25}$ to $R^{-2.47}$ so it decreases by about three orders of magnitude between the outer corona and $\epsilon = 90^{\circ}$. CME signal detection is background noise limited for all elongations, since the typical CME is $\sim 1\%$ of the natural background in the HI field of view. Additive instrumental backgrounds can further reduce sensitivity to the faint CME signal. Instrumental backgrounds due to stray photospheric light, cosmic rays incident on the solid state detector, improperly processed transverse stellar image motion, planets and earthshine (during the early part of the mission) are all potentially significant sources of instrumental background.

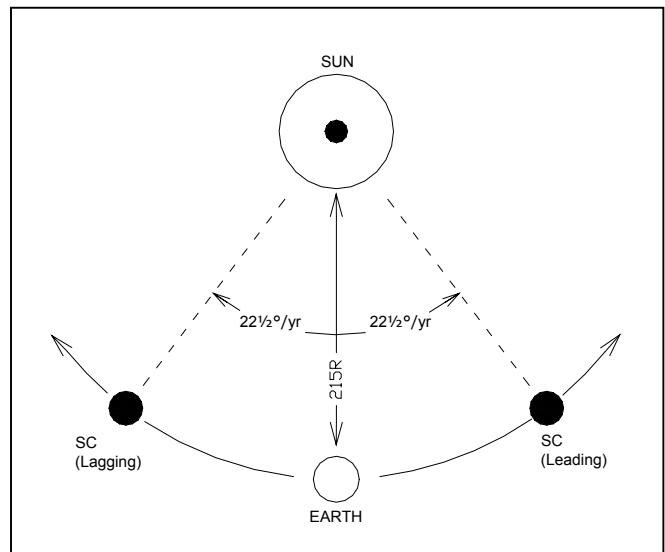


Figure 1. STEREO Mission orbit geometry

View from north ecliptic pole.

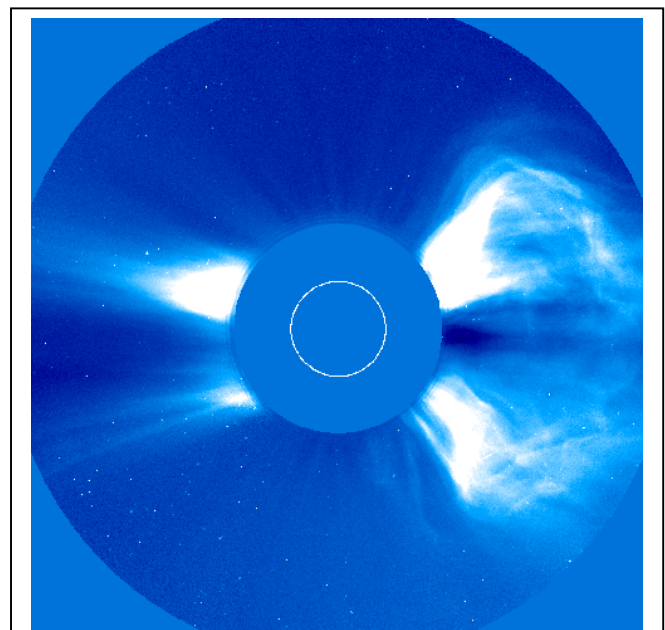


Figure 2. CME expected envelope

LASCO C2 white-light observations of a CME on 6 Nov 1997. Central circle represents the location of the solar limb.

The most appropriate instrumentation for CME observation changes with CME signal detection conditions and is thus a strong function of elongation. At small elongation, the relatively bright signal, narrow required field of view, and strong photospheric and coronal backgrounds suggest an externally occulted coronagraph. On the other hand, at high elongation, the extremely low CME signal, wide required field of view, and faint night sky suggest a heavily baffled, high light gathering power (LGP), and wide-angle all-sky telescope. The HI accommodates these disparate requirements with two specialized camera systems (HI-1 & HI-2) in a nested and progressively baffled mechanical structure.

2. OBSERVATIONAL PROBLEM

Properly executed, the HI provides the first opportunity to close the current $\sim 185 R_0$ wide geoeffective CME observation gap between the sun and the earth with high quality stereographic image pairs. The HI must be capable of detecting the extremely faint CME signal over a wide ($\sim 90^\circ$) field of view, which approaches within a few degrees of the bright solar disk and includes the bright earth. Rejection of the solar disk light is of paramount importance, since the natural object space background level (B) varies from 10^{-7} - 10^{-14} of the brightness of the solar disk (B_0) and the CME signal is only 10^{-2} of the night sky at high elongation, or $10^{-16} B_0$.

An ideal stereographic imaging instrument for the heliosphere inside $215 R_0$ would have a nearly sun centered hemispheric field of view. Such an instrument would allow simultaneous observation by both spacecraft of all CMEs in the heliosphere during the entire ~ 80 hours they reside within $215 R_0$. This comprehensive coverage would provide a data set suitable for the three-dimensional analysis of virtually all the CMEs that erupt over the duration of the STEREO mission. For a variety of technical reasons we chose a side looking, two-channel, sub-hemispheric field of view design instead. The side looking design has its field centers in the ecliptic plane at a moderate (HI-1) and at a high (HI-2) elongation (figure 3).

The basic observational problem for a side looking single lens design and the factors motivating the nested two-stage design proposed are illustrated in figure 4. The figure shows the cross-section of a single stationary, side looking, and nearly hemispheric field angle camera lens surrounded by a circular perimeter baffle. Two coupled geometrical optics problems arise with this concept. One problem has to do with the low LGP of the lens, which severely limits its utility in the dark sky regime. Only a small fraction of a very

wide-angle lens aperture gathers light from any given field direction (illustrated by the distinct ray bundles). Thus these lenses have low LGP for their physical aperture area and the fraction of the aperture area available for gathering light decreases rapidly with increasing field angle. When the lens is part of a camera, the LGP problem is coupled to the detector dimensions⁹. Thus if these lenses are used in a camera with a small format detector, the effective focal length must be kept short so that the very wide field angle image can be accommodated within the linear dimensions of the detector. This constrains the physical lens diameter used in the camera so that it cannot be scaled up to overcome the low LGP problem. For a very wide-angle lens used in conjunction with the 27.64 mm high spatial resolution SECCHI charge coupled device (CCD), the effective LGP could be comparable to a very small ~ 1 mm diameter aperture. Thus, for detection of the transient low brightness CME signal against the natural sky background at high elongation, the extremely low LGP of very wide-angle lenses presents a major problem.

The second problem for the single very wide-angle lens design has to do with instrumental background level. The Fresnel diffraction treatment for a straight edge indicates that the brightness of the diffracted light pattern behind a linear baffle varies approximately with the inverse square of the angle between a diffracted ray and the geometrical shadow line. The single

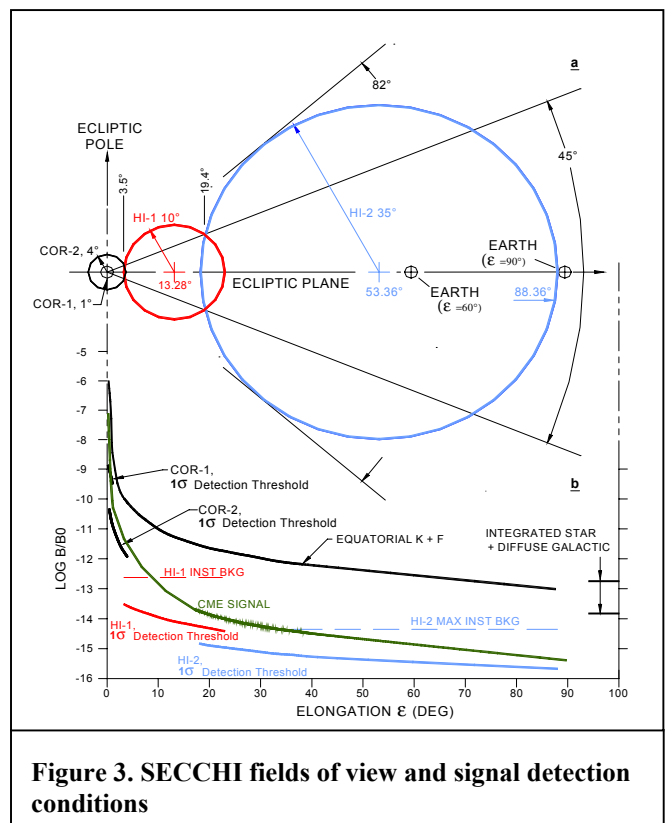


Figure 3. SECCHI fields of view and signal detection conditions

wide-angle lens background problem arises because part of the domed convex lens projects well up into the poor light rejection zone of the perimeter baffle shadow. This is the very part of the lens that must operate in the high elongation, dark, and poor signal detection region of the sky (figure 4). Lowering this part of the lens deeper into the baffle shadow is not possible because the baffle would then vignette the low elongation ray bundles. In a sense, the relationship between the geometrical optical properties of the lens and the geometry of the baffle system and its associated diffraction shadow pattern are inverted. Thus achieving a near sun view angle and a night sky instrumental background at large elongation with a single lens would be difficult. The single lens system also has little margin against the potential for catastrophic failure in the faint night sky portion of the celestial sphere, where the sky background is fourteen orders of magnitude below the brightness of the solar disk.

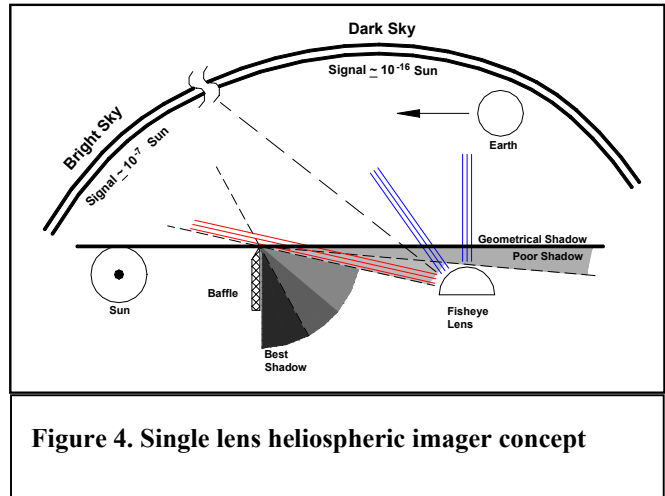


Figure 4. Single lens heliospheric imager concept

The above considerations led us view the observing problem and its instrumental solution as two distinct regimes. The relatively near sun, strong signal, bright sky, and small-angle field required in the small elongation regime suggested an externally occulted coronagraph. The low night sky brightness, extremely faint signal and wide-angle field required in the high elongation regime suggested a highly baffled, high LGP all-sky telescope. The inverted nature of the single very wide-angle lens approach and LGP problems could be rectified to a large degree by splitting the field of view into two regimes and observing each with separate intermediate-angle lenses in distinctly different baffle shadow locations. The HI accommodates these disparate requirements with two specialized camera systems (HI-1 and HI-2) in a nested two-stage baffle configuration (figure 5).

3. INSTRUMENT CONCEPT

The HI instrument shown in figure 5 is mounted on a side panel of the spacecraft whose normal is both in the ecliptic plane and perpendicular to the line of sight from the spacecraft to the sun. The roll angles of the two spacecraft differ by 180° so the panel normal on both the leading and the lagging spacecraft intersect the sun-earth line. HI is oriented on the panel so the optical axes of its two camera systems are in the ecliptic plane and intersect the sun-earth line.

The first stage of the HI baffle system is configured as a trapezoid located in a plane containing the line of sight from the spacecraft to the inner most field point off solar limb. The sun-facing base of the trapezoid is referred to as the linear forward baffle set while the top and two sides of the trapezoid are referred to as the perimeter baffle set. The function of the forward baffle set is to reject the solar disk, and to a lesser extent the inner corona, light from both the open interior of the trapezoid and the perimeter baffle system. The design approach can be understood by momentarily eliminating all the lead baffles in the multi-vane forward baffle set and substituting a single rectangular baffle for the last vane. The single rectangular baffle could be treated approximately as four half-screens bounded with linear edges casting four geometrical solar shadows. For a sample point, P, within the geometrical shadow and near the plane containing the trapezoid, one of the edges is totally obstructed by the closed interior of the HI structure. The three remaining edges define three reference solar geometrical shadow planes for the instrument, one over the open trapezoidal top and one along each of two sides. The perimeter baffle set is tapered in both width and height with respect to the three plane geometrical shadows cast by the forward baffle set. The taper angle, measured between the geometrical shadow line and the baffle, is the same for all three faces and of sufficient magnitude to reduce the diffracted solar photospheric light incident on the perimeter baffle to an acceptable level. The linear half-screen design for the forward baffle set was chosen in part because the single half-screen has the most rigorously developed diffraction description of any type of baffle and is among the most thoroughly tested. The degree of solar disk rejection afforded by the forward baffle can be computed using Fresnel's second order approximation to the Fresnel-Kirchhoff diffraction integral for a semi-infinite half-screen¹⁰. The multi-vane design of the forward baffle set for the three shadows is based on laboratory tested baffle system for a similar heliospheric imaging experiment¹¹. In the multi-vane approach, the vane edges are arranged in an arc such that the nth intermediate vane blocks the bright linear diffracting edge of the n-1 vane from the view of the n+1 vane edge. Fresnel's approximation can be applied to this arrangement as a cascade. Note that the last vane in the cascade is the only vane edge directly illuminating the perimeter baffle and the interior of the

trapezoid. Thus the single baffle approximation described above is geometrically accurate, since the preceding vanes in the set serve only to reduce the solar photospheric intensity incident on the three edges of the final vane.

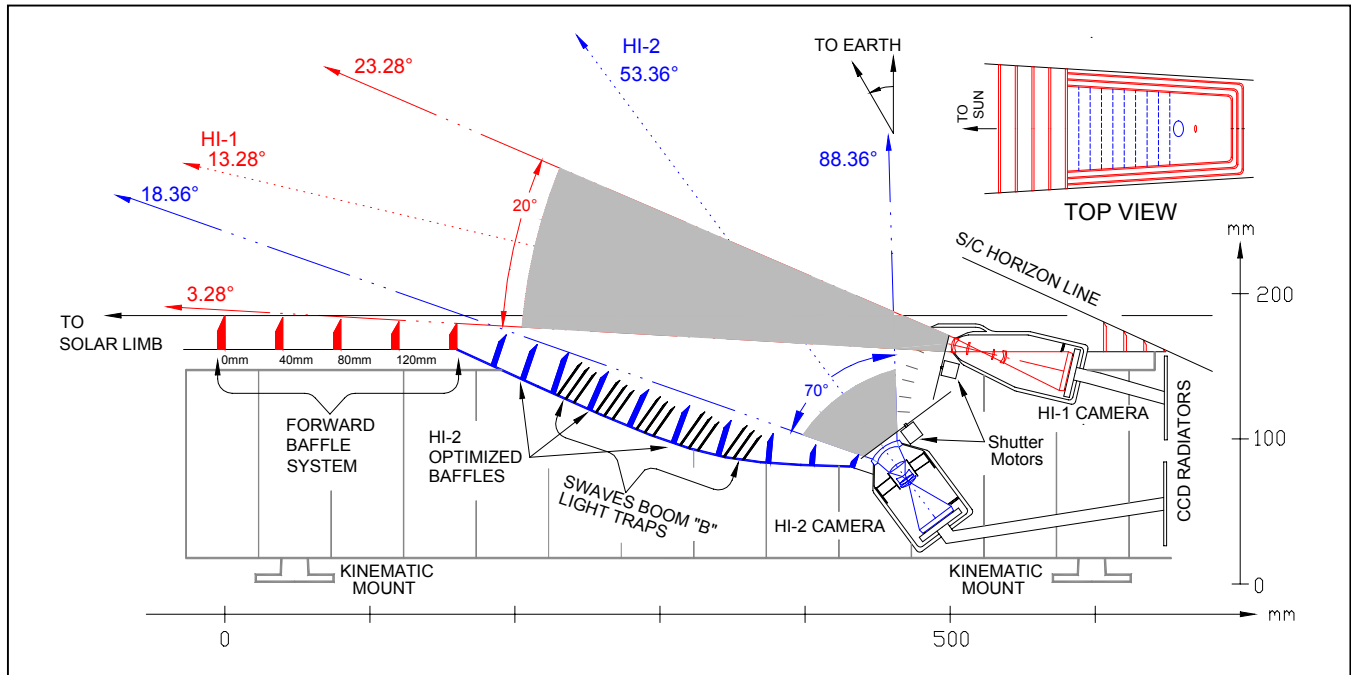


Figure 5. SECCHI Heliospheric Imager Concept

The main function of the three-sided perimeter baffle set is to protect the interior of the first and second stage baffle systems from solar photospheric light reflected or scattered from the spacecraft. All spacecraft elements, with one exception, are required to remain below the extension of the trapezoidal baffle plane. The one exception is a single six meter long monopole antenna, one of the three nearly orthogonal monopoles deployed by the STEREO/WAVES (SWAVES) experiment low frequency radio receiver. Calculations indicate that scattered photospheric light from this monopole, which is directly illuminated by the solar photosphere, can be adequately trapped in the interior of the HI baffle system. Part of the reason for designing the HI as a side looking and sub-hemispheric instrument rather than a side looking and hemispheric instrument was to accommodate such a three orthogonal antenna radio instrument.

The HI-1 camera utilizes a moderate 20° full field angle camera, centered 13.28° (~50 R₀) from the solar disk, a 2048x2048 pixel format CCD and the first stage of the two-stage HI baffle system. The heights of the linear edges of the five vane forward baffle are arranged along a section of a circle whose tangents at the first and the last vanes intersect the solar limb and the top edge of the HI-1 lens aperture respectively. The last vane of the forward linear baffle system is the only edge visible to the HI-1 lens. It is imaged by the lens near a matching linear internal occulter coated with a highly absorbing material. The image plane of the external occulter is also slightly behind the internal occulter and the CCD front surface. However, since the distance from the last forward baffle vane to the lens is much greater than the focal length of the lens, the external occulter defocus at the internal occulter is minimal. HI-1 is similar to an externally occulted coronagraph but without either a Lyot stop or a Lyot spot. A small baffle over the top of the objective lens protects it from earthshine. Diffraction measurements^{11,12} and Fresnel diffraction integral calculations¹⁰, with the forward baffle vane height distribution optimized for the HI-1 lens, indicate an instrumental background $\leq 3 \times 10^{-13}$ B/B₀ at the inner field cut off, $\epsilon = 3.28^\circ$ (12.3 R₀), will be achieved. This is substantially below the natural K+F corona background in the small elongation bright sky regime and a factor of 10 better than the $< 10^{-12}$ B/B₀ achieved on SOHO LASCO/C3¹³. The improvement over LASCO/C3 is due primarily to the substantially greater HI-1 inner field of view cutoff (12.3 R₀ vs. 3.8 R₀) and the fact that the Fresnel diffraction pattern intensity varies approximately with the inverse square of the diffraction angle.

The HI-2 camera uses a wide 70° full field angle objective set deep within the forward baffle set shadow at a diffraction angle of 16.5° (upper solar limb to lens top edge), where the HI-1 forward baffle Fresnel diffraction calculation result is 2.3×10^{-18} B/B₀, well below the required 10^{-14} B/B₀. This location rectifies the inverted geometry problem associated with a single lens system (figure 4). The HI-2 system is akin to a wide-angle night sky camera. In order to minimize solar stray light rejection risk further, the HI-2 baffle system is progressively staged with the HI-1 in the sense that the last vanes in the first stage baffle system constitute the light sources incident on the rather similar second stage baffle system. The HI-2 camera and uses a second stage forward baffle matching internal occulter-stop located at the focal plane. There is also a separate inter-camera baffle system between the HI-1 and HI-2 apertures to block light incident on the HI-1 camera face and its earthshine baffle from scattering into the HI-2 entrance aperture. The HI-2 camera consists of a wide-angle (rather than a very wide-angle) fisheye lens and a 2048x2048 pixel format CCD. The field angle compromise results in an effective LGP aperture diameter of about 7 mm on-axis. The HI-2 instrumental background is dominated by veiling glare from earthshine diffracted at the objective aperture stop rather than baffle diffracted solar light. The instrumental background is 5×10^{-15} B/B₀ for a spacecraft-earth lead (lag) angle of 2° and thereafter diminishes approximately as the inverse square of the spacecraft-earth distance.

In summary, by using a second camera aperture at a large diffraction angle, additional staged baffling and a 70° wide angle lens with greater LGP than a hemispherical field angle lens, we mitigate stray light rejection risk, improve threshold background noise limited signal detection at high elongation, and reduce the required overall dimensions of the perimeter baffle. The superior diffraction angle afforded the night sky portion of the field in this design is important since solar stray light rejection is the paramount risk. This approach to technical risk mitigation is driven by the fact that the empirically determined baffle diffraction performance has not been established below about 10^{-8} for wide-angle type diffraction baffle systems¹¹. However Fresnel diffraction calculations indicate that the solar disk driven instrumental background of HI is below the natural object space background for all elongations within the respective fields of view (figure 3). This performance will have to be verified during instrument development. The HI characteristics are presented in table 1.

	HI-1 Characteristics	HI-2 Characteristics
Field of View		
Half angle	10°	35°
Center	49.8R (13.28°)	200R (53.36°)
Inner Cutoff (Unvignetted)	12.3R (3.28°)	72.8R (19.4°)
Outer Cutoff (Unvignetted)	87.3R (23.28°)	332R (88.6°)
CCD Format	2048x2048x13.5μ	2048x2048x13.5μ
Plate scale	35.15"/pixel	2.05"/pixel
Objective	AR coated	AR coated
Diameter	16.0 (16) mm	20.7 (7.01) mm
Focal length	78.4 mm	19.74 mm
F-ratio	f/4.9	f/2.8
Passband	6500 Å - 7500 Å	4000 Å - 10000 Å
Instrumental background	< 3×10^{-13} B/B ₀	< 5×10^{-15} B/B ₀
Nominal exposure time	12 sec	60 sec
SNR	$\geq 30/(\text{pixel} \cdot \text{hr})^{1/2}$	$\geq 15.5/(\text{pixel} \cdot \text{hr})^{1/2}$

Table 1. HI instrument characteristics

4. INSTRUMENT OPERATION

Individual (single shutter open/close cycle) HI-1 exposure times are 12 sec at ≤ 50% CCD saturation and HI-2 exposure times are 60 seconds at ≤ 40% CCD saturation. Individual exposures, separated only by the CCD read time (4.2 sec) are acquired continuously with both cameras and each camera image stream is digitally integrated in a 32 bit deep image buffer memory by a dedicated processor for ~20 minutes on HI-1 and ~60 minutes on HI-2. The integration develops a pair of high signal to noise ratio images (~21 bits/pixel deep) from HI-1 and HI-2 for insertion into the STEREO telemetry stream at the respective 20 minute and 60 minute cadences.

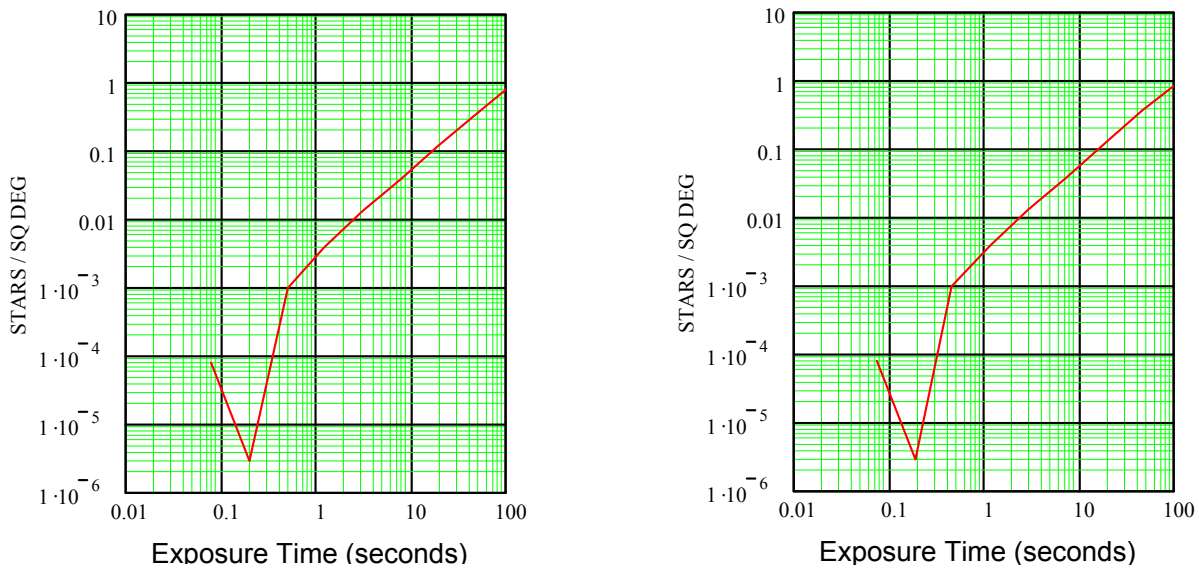


Figure 6. Spatial density distribution of saturating stars

The spatial density distribution of saturating stars is shown as a function of individual exposure times for the HI-1 (6a, left) and HI-2 (6b, right).

The impact of bright stars in the field of view has been calculated for both HI-1 and HI-2 based on the apparent magnitude star count table in Allen¹⁴. Figure 6 shows the spatial density of CCD pixel saturating stars as a function of a single shutter cycle exposure time for HI-1 (6a) and HI-2 (6b). In HI-1, stars brighter than visual magnitude ~ 5 , spatial density $\sim 0.07/\text{deg}^2$, will saturate and stars brighter than visual magnitude ~ 3 , spatial density $\sim 0.0037/\text{deg}^2$, will bloom. Thus on average there will be about 1.2 blooming stars in the HI-1 field. In HI-2, stars brighter than visual magnitude ~ 7 , spatial density $\sim 0.5/\text{deg}^2$, will saturate and stars brighter than visual magnitude ~ 5 , spatial density $\sim 0.07/\text{deg}^2$, will bloom. Thus there will be about 85 blooming stars in the HI-2 field on average. The saturated and bloomed pixels are not photometric. These bright stellar defect portions of the images will be corrected with post processing trans-defect interpolation on the ground. We expect the correction to be reasonably accurate since the defects occupy only a small fraction of the field of view. This is an important correction however because a point defect in one stereo image maps into a one-dimensional virtual line defect in its stereographic conjugate image during the three-dimensional reconstruction process. Thus, when the stereograms are used for three-dimensional coronal or heliospheric object reconstruction, uncorrected stellar defects map into two-dimensional planar defects in object space. Several planets are also relatively bright blooming sources. They will be treated in much the same manner as stars.

Cosmic ray impacts on the CCD constitute a significant instrumental background that must be addressed on board. We analyzed the problem using the nominal cosmic ray flux ($6.2 \text{ events}/\text{cm}^2/\text{sec}$) and characteristic CCD electron charging ($\sim 10^3$ electrons/event) recorded by the SOHO/LASCO CCDs along with the simplifying approximation that the entire cosmic ray generated charge is deposited in a single pixel. The mean time between consecutive cosmic ray hits in a given pixel is about 24 hrs, so multiple hits in a single pixel during the exposure plus read time (16.2 and 64.2 seconds) can be ignored. Figure 7 compares the cosmic ray generated charge and the detected equatorial and polar photon *noise* charge for nominal HI-1 and HI-2 integrated exposure time of 14.8 min (74 exposures, 20 minute integration cadence) and (56 exposures, 60 minute integration cadence) respectively. In both HI-1 and HI-2 the natural background photon noise dominates the cosmic ray charge at small elongations while the cosmic ray charge dominates the photon noise at high elongations. The fraction of pixels affected in the summed image is about 1% and 4% for HI-1 and HI-2 respectively.

The cosmic ray impact data indicates that, while cosmic rays must be scrubbed because they contribute a significant noise background, they are not an overwhelming problem. The main concern is to remove them without introducing systematic errors. We plan to scrub each individual exposure for cosmic rays on-board, before integrating into the 32 bit deep memory

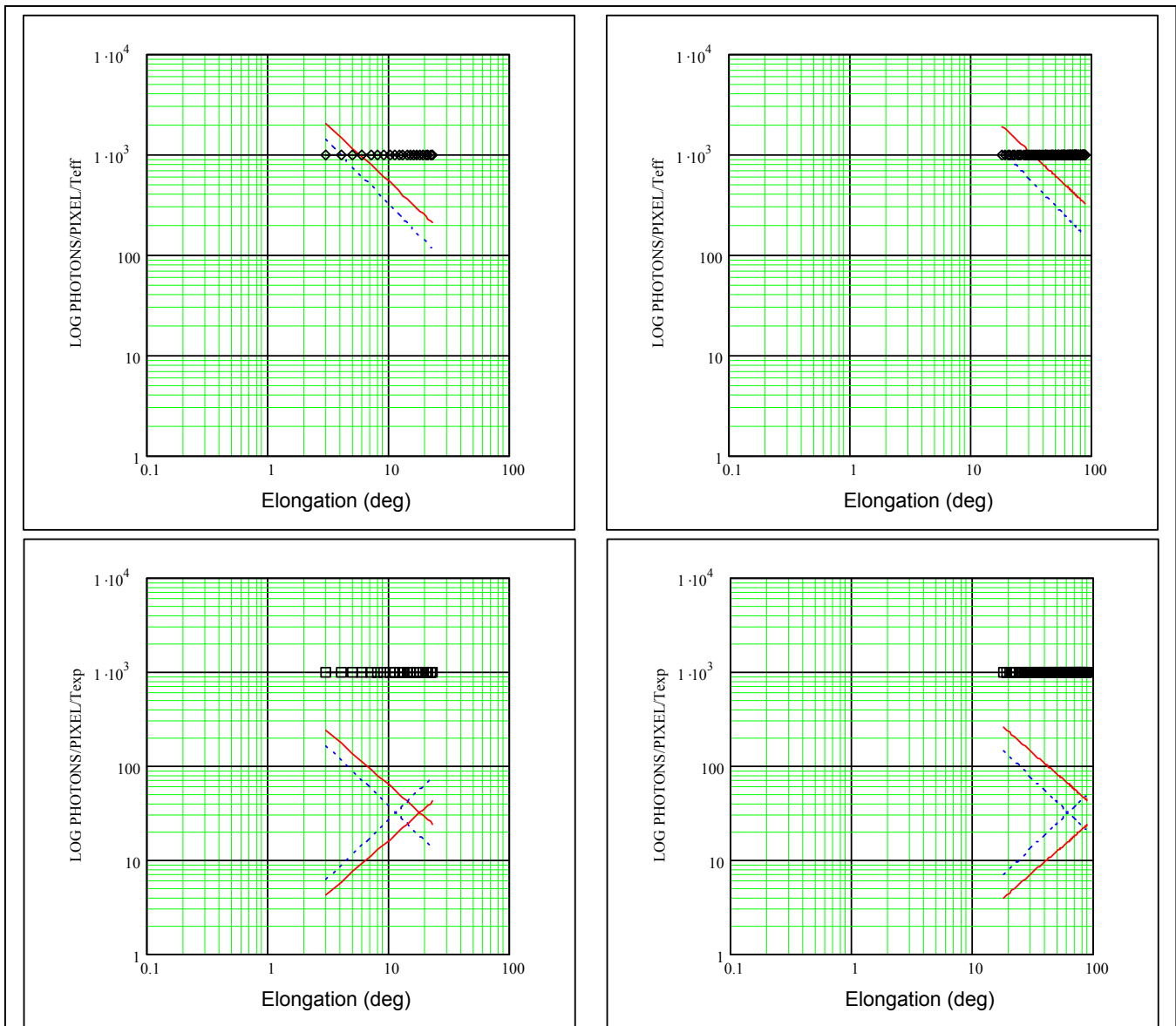


Figure 7. Cosmic ray effects

The cosmic ray “signal” (diamonds) in impacted pixels compared to the equatorial (solid) and polar (dashed) rms photon noise backgrounds for HI-1 (7a, upper left) and HI-2 (7b, upper right) for the standard HI-1 12 sec x 74 and HI-2 60 sec x 56 intergrated exposures. The cosmic ray “signal” (boxes) in impacted pixels compared to the equatorial (solid) and polar (dashed) rms photon noise backgrounds for HI-1 (7c, lower left) and HI-2 (7d, lower right) for the standard single HI-1 12 sec x 1 and HI-2 60 sec x 1 exposures (negative slopes) and the cosmic ray signal to photon noise ratio (positive slopes).

and before pixel binning, by executing a pixelwise running comparison of three consecutive images. The i,j pixel in the n^{th} CCD image that has a charge value well above the i,j pixel charge values in the $n-1$ and $n+1$ CCD image will have its value in the n^{th} image set to its average value derived from the $n-1$ and $n+1$ images. Figures 7c, 7d compare the cosmic ray charge with the solar equatorial and polar photon noise for single (12 second and 60 second) exposures in HI-1 and HI-2. The cosmic ray “signal” to photon noise ratio is also plotted. The plots show that the cosmic ray detection threshold can be set at a fairly high level ($\sim 5\sigma$) so that the algorithm will not be very sensitive to either photon noise or slow stellar transpixel migration induced variations. The cosmic ray contributions below this threshold will be less significant than the photon noise

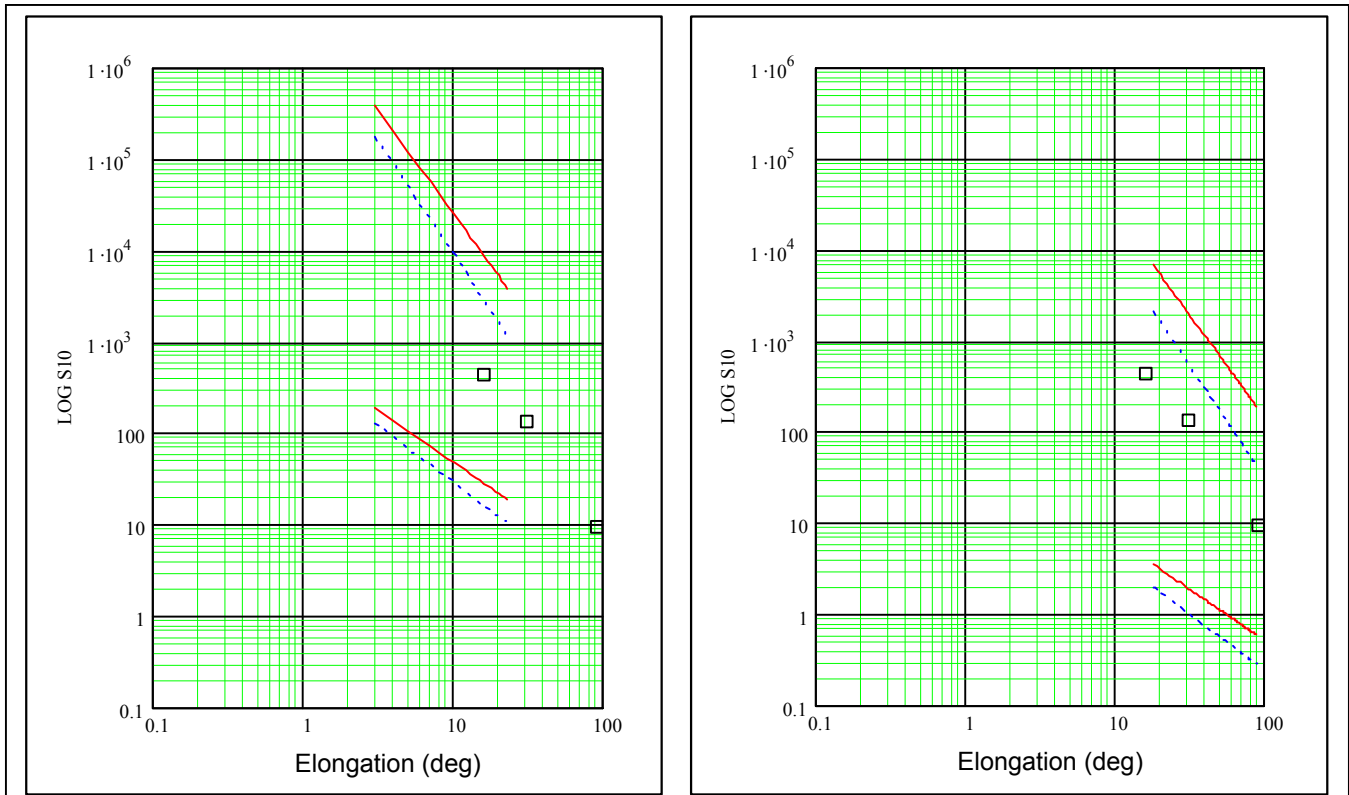


Figure 8. Single pixel CME signal, natural background and natural background noise level

CME signal, natural background and natural background noise level (in S10 units) as a function of elongation ϵ are shown for HI-1 (8a, upper left) and HI-2 (8b, upper right). The CME signal from the three HELIOS channels is shown (boxes) for the subset of CMEs that were observed in all three channels⁵. Selecting the three channel CMEs provides the brightness elongation profile but also biases the selection to the brighter CMEs. The equatorial (solid) and polar (dashed) natural backgrounds (upper lines) and their rms noise (lower lines) are also shown for single pixel and standard HI-1 12 sec x 74 and HI-2 60 sec x 56 integrated exposures. The system detection margins should allow detection of faint CMEs.

in the integrated images. After cosmic ray scrubbing, the 14 bit precision ADC single CCD images will be accumulated to ~21 bits in the 32 bit deep image buffer memory. At the present time we plan to execute the scrub and sum task for both HI-1 and HI-2 on a dedicated processor board with 32 Mbytes of memory. Trial runs of several cosmic ray scrub algorithms using LASCO/C3 image sequences indicate that the scrub should work well.

5. EXPECTED PERFORMANCE

A high quality image is important for the stereographic reconstruction process. Stereographic image pairs used in reconstruction must be radiometrically consistent and have high signal to noise ratios. Radiometric consistency can be satisfied with a stable CCD camera, a repeatable shutter motion, a good preflight flat field calibration of the CCD cameras and a lens design exhibiting minimal ghosts of moving objects such as planets.

Both photon statistics and CME proper motion affect image spatial resolution. The photon statistical resolution can be estimated with a signal to noise ratio (SNR) image quality metric¹⁵. The metric can be calculated from the signal, scene and instrumental backgrounds, camera properties, and the operating conditions. For HI-1 the operating conditions are 12 second individual exposures, 4.2 second read, 74 integrated individual exposures for a total of 14.8 minutes integration time and 20 minute digitally integrated image cadence. Similarly for HI-2 the operating conditions are 60 second individual exposures, 4.2 second read, 56 integrated individual exposures for a total of 56 minute integration time and 60 minutes digitally integrated image cadence. The calculation results are shown in figure 8. The lower curves in figure 8a, 8b show the single CCD pixel 1σ precision for photons accumulated during the integrated exposures. It can be seen that the poorest ratio of the

CME signal to rms photon noise is about 15σ in both HI-1 (@ $\epsilon = 23.28^\circ$) and HI-2 (@ $\epsilon = 88.6^\circ$). CME proper motion is $\sim 1^\circ/53$ min, so a 48 minute exposure with a 32×32 CCD pixel binned superpixel resolution element matching CME travel would have a SNR greater than or equal to $\sim 444 \sigma$. A SNR ~ 5 per spatial resolution element is required for threshold detection of a simple known a-priori target^{15,16} and substantially higher photon statistics ($\geq 30\sigma$) are required for more complex images¹⁷ and, presumably, good stereographic reconstruction. A convenient estimator of spatio-temporal image SNR is to multiply the (number of binned pixels x integrated exposure time)^{1/2} x 30 (HI-1) or x 15.5 (HI-2).

ACKNOWLEDGEMENTS

STEREO/SECCHI/HI is funded under NASA contract S-13631-Y.

REFERENCES

1. R.A. Howard, G.E. Brueckner, O.C. St.Cyr, D.A. Biesecker, K.P. Dere, M.J. Koomen, C.M. Korendyke, P.L. Lamy, A. Llebaria, M.V. Bout, D.J. Michels, J.D. Moses, S.E. Paswaters, S.P. Plunckett, R. Schween, G.M. Simnett, D.G. Socker, S.J. Tappin, D. Wang, "Observations of CMEs from SOHO/LASCO," *Coronal Mass Ejections*, N. Crooker, J.A. Joselyn, J. Freeman, editors, The American Geophysical Union, pp. 17-26, 1997.
2. A.J. Hundhausen, "An Introduction," *Coronal Mass Ejections*, N. Crooker, J.A. Joselyn, J. Freeman, editors, The American Geophysical Union, pp. 1-7, 1997.
3. C. Leinert and D. Kluppelberg, "Stray Light Suppression in Optical Space Experiments," *Applied Optics*, **13**, pp. 556-564, 1974.
4. I. Richter, C. Leinert, and B. Planck, "Search for Short Term Variations of Zodiacal Light and Optical detection of Interplanetary Plasma Clouds," *Astronomy and Astrophysics*, **110**, pp. 115-120, 1982.
5. D.F. Webb and B. V. Jackson, "The Identification and Characteristics of Solar Mass Ejections Observed in the Heliosphere by the Helios 2 Photometers," *Journal of Geophysical Research*, **95**, pp. 20641-20661, 1990.
6. B.V. Jackson, A. Buffington, P.L. Hick, S.W. Kahler, R.C. Altrock, R.E. Gold, and D.F. Webb, "The Solar Mass Ejection Imager", in *Solar Wind Eight*, D. Winterhalter, J. T. Gosling, S. R. Habal, W. S. Kurth, and M. Neugebauer, eds., AIP Conf. Proc. **382**, pp. 536-539, 1996.
7. S. Koutchmy and P.L. Lamy, "The F-corona and the circum-solar dust evidences and properties," in "Properties and Interactions of the Interplanetary Dust," IAU Colloq. **85**, pp. 63-74, 1985.
8. C. Leinert, I. Richter, E. Pitz, and B. Planck, "The Zodiacal Light from 1.0 to 0.3 A.U. as Observed by the Helios Space Probes," *Astronomy and Astrophysics*, **103**, pp. 177-188, 1981.
9. A. Buffington, "Very-wide-angle optical systems suitable for spaceborne photometric measurements," *Applied Optics*, **37**, pp. 4284-4293, 1998.
10. M. Born and E. Wolf, *Principles of Optics*, 6th (corrected) edition, Pergamon Press, New York, 1980.
11. Buffington, A. Jackson, B.V. and Korendyke, C.M., "Wide-angle stray-light reduction for a spaceborne optical hemispherical imager," *Applied Optics*, **35**, No. 34, pp. 6669-6673, 1996.
12. M. Romoli, H. Weiser, L.D. Gardner and J.L. Kohl, "Stray light suppression in a reflecting white light coronagraph," *Applied Optics*, **32**, pp 3559-3569, 1993.
13. G.E. Brueckner, R.A. Howard, M.J. Koomen, C.M. Korendyke, D.J. Michels, J.D. Moses, D.G. Socker, K.P. Dere, P.L. Lamy, A. Llebaria, M.V. Bout, R. Schwenn, G.M. Simnett, D.K. Bedford, C.J. Eyles, "The Large angle spectroscopic coronagraph (LASCO)," *Solar Physics*, **162**, pp. 357-402, 1995.
14. C.W. Allen, *Astrophysical Quantities*, 3rd edition, The Athlone Press, London, 1976.
15. A. Rose, "The Sensitivity Performance of the Human Eye on an Absolute Scale," *Journal of the Optical Society of America*, **38**, No. 2, pp. 196-208, 1948.
16. H.H. Barrett, "Objective assessment of image quality: effects of quantum noise and object variability," *Journal of the Optical Society of America*, A., **7**, No. 7, pp. 1266-1278, 1990.
17. A. Rose, "Quantum and Noise Limitations of the Visual Process," *Journal of the Optical Society of America*, **43**, No. 9, pp. 715-716, 1953.